UC Irvine
UC Irvine Previously Published Works

Title

Maximum a posteriori classification of multifrequency, multilook, synthetic aperture radar intensity data

Permalink

Journal

ISSN

Authors

Rignot, E
Chellappa, R

Publication Date

DOI

Copyright Information

Peer reviewed

Maximum *a posteriori* classification of multifrequency, multilook, synthetic aperture radar intensity data

E. Rignot

Jet Propulsion Laboratory, California Institute of Technology, Pasadena, California 91109

R. Chellappa

*Department of Electrical Engineering, Center for Automation Research, University of Maryland,
College Park, Maryland 20742*

We present a maximum *a posteriori* (MAP) classifier for classifying multifrequency, multilook, single polarization, synthetic aperture radar (SAR) intensity data into regions or ensembles of pixels of homogeneous and similar radar backscatter characteristics. A model for the prior joint distribution of the multifrequency SAR intensity data is combined with a Markov random field for representing the interactions between region labels to obtain an expression for the posterior distribution of the region labels given the multifrequency SAR observations. The maximization of the posterior distribution yields Bayes's optimum region labeling or classification of the SAR data or its MAP estimate. The performance of the MAP classifier is evaluated by using computer-simulated multilook SAR intensity data as a function of the parameters in the classification process. Multilook SAR intensity data are shown to yield higher classification accuracies than one-look SAR complex amplitude data. Examples using actual two-frequency, four-look, SAR intensity data acquired by the NASA/Jet Propulsion Laboratory airborne polarimetric SAR are presented. The MAP classifier is extended to the case in which the radar backscatter from the remotely sensed surface varies within the SAR image because of incidence angle effects. The results obtained illustrate the practicality of the method for combining SAR intensity observations acquired at two different frequencies and for improving classification accuracy of SAR data.

1. INTRODUCTION

Techniques for segmenting synthetic aperture radar (SAR) images are essential for the development of automated computer systems capable of handling and analyzing, at high data rates, a large volume of SAR observations of the Earth and other planets from a spaceborne sensor. Segmentation techniques help to condense the information contained in the SAR images, help to detect and map scene features of interest for subsequent image analysis and scene description, and facilitate the inference of geophysical and biophysical parameters of various types of surfaces from SAR data by using inversion techniques.[1]

In this paper we present a technique for classifying multifrequency, multilook SAR intensity data into regions or ensembles of pixels of homogeneous and similar radar backscatter properties. Given multifrequency, multilook SAR intensity measurements at each pixel location of a data array and a model describing the statistical distribution of these measurements, we want to label, in some optimum fashion, each image pixel s with a region label $L_s \in \{1, \ldots, K\}$, where K is the number of regions and where, for instance, $L_s = 2$ means that the image pixel indexed s belongs to region 2. The radar backscatter characteristics of each region are assumed to be known in advance, from a supervised selection of the regions of interest, from a multidimensional clustering analysis of the SAR data, or from a combination of both.

Rignot and Chellappa[2] presented a maximum *a posteriori* (MAP) Bayesian classification technique for classifying single-frequency, single polarization, one-look SAR complex amplitude data into homogeneous regions. It was shown that the inherent high-order statistics of the SAR signal (namely, the correlation properties of the complex amplitudes) could be successfully incorporated into a statistical model for representing the SAR complex measurements and that the combination of this model with a Markov random field (MRF) for representing the prior distribution of the region labels of the data could yield an algorithm with high classification quality and accuracy. In this paper we extend the technique developed for one-look SAR complex amplitudes to the case of multilook SAR intensity data for which the statistics of the signal are significantly different and modeling requires major modifications.

SAR complex amplitudes (that is, amplitude and phase of the radar return) are produced in the last stage of SAR processing following compression of the data in both the range and azimuth directions[3] and correspond to a single sample or a so-called look of the scene. At each pixel location s, the complex amplitude, denoted $\mathbf{a}_s$, may be detected to generate a one-look intensity image, where the intensity at each pixel location is the squared magnitude of the amplitude (that is, where $I_s = |\mathbf{a}_s|^2$). One inconvenience of one-look intensity data is that the variance of the intensity is large and proportional to the squared mean intensity level because of the presence of image speckle, a consequence of the interference of returns from independent scatterers within a resolution cell of the coherent imaging system. The large variance of one-look SAR intensity data renders their visual analysis difficult. One-look SAR data are therefore often considered intermediate

products, and postprocessing techniques, called multilooking techniques, are applied to them to produce multilook SAR intensity data. The idea is to form an image that represents the average of several independent samples or looks of the scene. There are several ways to obtain multilook images.[4,5] The multilooking techniques implemented in practice involve only one data take. Typically, N single-look complex amplitudes $\mathbf{a}_p$ with $p \in \{1, \ldots, N\}$ are selected from either time or spectral division of the one-look SAR data, detected (that is, compute $I_p = |\mathbf{a}_p|^2$) and incoherently averaged (that is, $I = \Sigma_{p=1}^{p=N} I_p/N$). N is the number of looks. The process is done at the expense of spatial resolution, which is degraded by a factor N.[4,5] In addition, the phase of the radar return is lost during multilooking because of detection and incoherent averaging. The advantages of multilooking are that the variance of the intensity is reduced by a factor N, visual analysis of the SAR images is facilitated, and the data volume is divided by $8N$ because multilook intensity data can be coded on 8 bits (instead of 64 bits for complex amplitude data) with minimal information loss.

Methods that were developed previously for classifying multilook SAR intensity data suffer many drawbacks. These techniques are basically divided into two categories: (1) techniques based on speckle removal as a preprocessing step and thresholding of the intensity level for classification[6] and (2) the gray level co-occurrence matrix (GLCM) method,[7] a statistical approach based on the first- and second-order statistics of the signal. A variety of filters for removing image speckel have been proposed. These filters decrease speckle by using statistics calculated from a local support neighborhood, assuming homogeneous scattering characteristics. However, speckle removal, originally developed for display purposes and based on an approximate image model, degrades spatial resolution and the information content of the data, sometimes in a nonuniform manner across the image. The GLCM method, in contrast, ignores image speckle that dominates the statistics of the signal and is falsely interpreted as a natural textural variability of the radar response from the imaged surface, which varies proportionally to the mean intensity level of the radar return. The selection and estimation of the classification parameters in the GLCM method are also scene dependent and computationally expensive. Segmentation results based on either technique appear noisy and are not satisfactory for practical applications.

In this paper we present a MAP Bayesian classifier adapted to the first- and second-order statistical characteristics of multilook, single polarization, SAR intensity data. The classification technique is extended to the case in which SAR observations are made at different frequencies of the radar electromagnetic signal. Several spaceborne SAR instruments will be launched in upcoming years to gather radar data about the Earth's surface and environment at a single frequency and polarization but with radars operating at distinct frequencies and polarizations. It is possible that those SAR data could be used in a synergistic manner. Multifrequency SAR observations significantly increase our capability to separate and to characterize different types of natural surfaces compared with single-frequency measurements in geology, sea-ice monitoring, and forestry studies.[8] The technique

presented in this paper could be of direct use for classifying SAR data acquired by several of these spaceborne sensors, provided that the multifrequency SAR data are first spatially coregistered on a pixel-by-pixel basis.[9]

In addition to the multifrequency capability, the classifier presented in this paper has a multiple incidence angle capability, that is, it is adapted to the case in which the radar backscatter from natural surfaces varies within the image because of incidence angle effects. This situation is commonly encountered in SAR imagery, and any type of classifier must account for incidence angle effects to operate correctly on the data. The incidence angle of the radar electromagnetic signal onto the surface varies within one scene because of the SAR imaging geometry and of spatial variations in surface slopes owing to the presence of topography. The radar cross section of natural surfaces decreases significantly with an increasing incidence angle,[10] and the rate of decrease depends on the type of surface cover.

The paper is organized as follows. In Section 2 the first- and second-order statistics of the multilook SAR intensity data are duscussed, a model for their prior joint distribution is proposed, and an MRF model for the prior distribution of the region labels is given. In Section 3 an expression for the posterior distribution of the region labels given the SAR observations is derived, and the MAP criterion is formulated. In Section 4 we discuss the effects on classification accuracy of the number of looks and of the spatial variability of the radar cross section of natural surfaces (that is, texture), using computer-simulated multilook SAR intensity data. A generalization of the MAP technique to the multifrequency case is given in Section 5. Its adaptation to incidence angle dependent backscatter characteristics is discussed in Section 6. In Section 7 an example of the application of the MAP classification technique by using actual, two-frequency, four-look, SAR intensity data of sea ice acquired by AIRSAR is presented. Section 8 concludes the paper.

2. IMAGE MODEL AND MATHEMATICAL ASSUMPTIONS

A. Image Model for the SAR Intensity Data
A Bayesian approach requires a model of a prior knowledge of the distribution of the observed variables. Although an expression for the prior marginal distribution of the intensity data would suffice for that purpose, it is better to obtain an expression for the prior joint distribution of M intensity values contained in a neighborhood N_s whose center is pixel s, where s is an element of the data array Ω. In this manner, additional correlated information from neighboring pixels is incorporated into the statistical model, and better classification results are subsequently obtained.[2] In this section we successively examine the marginal distribution, the correlation properties, and the joint distribution of multilook SAR intensity data.

1. Marginal Distributions
In contrast to the case of one-look, SAR complex amplitudes, the marginal distribution of multilook, SAR intensity data is not accurately known because multilooking is a nonlinear process often performed on one-look data samples that are slightly correlated. When one-look com-

plex samples selected for multilooking are independent random variables and the backscatter cross section of the imaged surface, denoted σ°, is locally uniform, it is well known that the multilook intensities are gamma distributed[11] as

$$p(I_s/L_s) = \frac{N^N I_s^{N-1}}{\langle I \rangle_l{}^N \Gamma(N)} \exp\left(-\frac{N I_s}{\langle I \rangle_l}\right), \qquad (1)$$

where the angle brackets denote the spatial average operator and N is the number of independent one-look samples used to form each multilook intensity sample I_s. The spatial average of the intensity in region l, denoted $\langle I \rangle_l$, is a constant proportional to the value of σ° in region l.

If the backscatter cross section σ° is nonuniform but spatially varying (that is, textured) within each region, $\langle I \rangle_l$ is a random variable. When $\langle I \rangle_l$ is gamma distributed with parameter α_l, the multilook intensities are K distributed[12,13]:

$$p(I_s/L_s) = \frac{2\alpha_l N}{\Gamma(\alpha_l)\Gamma(N)\langle I \rangle_l}\left(\frac{\alpha_l N I}{\langle I \rangle_l}\right)^{\alpha_l+N-2/2}$$
$$\times K_{\alpha_l-N}[2(\alpha_l I/\langle I \rangle_l)^{1/2}], \qquad (2)$$

where $K_{\alpha_l-N}()$ is the modified Bessel function of the third kind of order $(\alpha_l - N)$. K distributions describe the statistics of SAR data better in the presence of texture.[14,15]

However, if the number of looks N in Eq. (1) is arbitrarily modified to match the observed larger-than-expected variance of the intensity (owing to the textural variability of σ°), gamma distributions still model the statistics of multilook SAR intensity data reasonably well[16] and have the advantage of a simpler analytical expression.

When the one-look samples selected for multilooking are correlated, and they often are because of sampling of the SAR data versus the spatial width of the SAR coherent impulse response, Eqs. (1) and (2) are not mathematically correct. The exact form of the distribution does not have a simple closed-form expression.[11] A computationally convenient alternative is to adapt the number of looks N in Eqs. (1) and (2) to model the slightly larger-than-expected variance of the signal. Again, gamma distributions have the advantage of a simpler analytical expression.

2. Correlation Properties of Multilook Intensity Data
The correlation properties of one-look complex amplitude data depend only on the coherent impulse response h of the SAR imaging and processing systems.[2] They are not affected by the focusing of the SAR system or by the spatial variability of the backscatter cross section of the surface.[17] The situation is completely different in the case of multilook SAR intensity data, as both focusing of the SAR instrument and the natural textural variability of the surface have an effect. In this section we derive a simple expression to quantify the effects of texture on the correlation properties of multilook intensity data. The effects of misfocusing the radar are also briefly discussed.

Let us consider the general case of a nonstationary scene. We view the scene as composed of a set of regions or ensembles of contiguous pixels for which the average backscatter characteristics are similar. In each of these

regions we assume the existence of a spatial mean value $\langle I_s \rangle$ of the signal and of a spatial average autocorrelation function of the intensity $[R_I(s, s + \mathbf{r}) = \langle I_s I_{s+\mathbf{r}} \rangle]$, where $\mathbf{r}$ is a two-dimensional displacement vector in the image plane. To account for the spatial variability of $\langle I_s \rangle$, the spatial mean value of the signal is modeled as

$$\langle I_s \rangle = T_l(s)\langle I \rangle_l, \qquad (3)$$

where $\langle I \rangle_l$ is a constant in region l and T_l is a normalized texture random variable ($E[T_l] = 1$, where E denotes the expected value), with stationary statistics. T_l represents the random fluctuations of the backscatter cross section σ° of the surface owing to local inhomogeneities in region l. The autocorrelation function of the N-look intensity is, in region l,

$$R_{I_l}(s, s + \mathbf{r}) = \left\langle \frac{1}{N}\sum_{p=1}^{p=N} I_p(s)\frac{1}{N}\sum_{q=1}^{q=N} I_q(s + \mathbf{r})\right\rangle$$
$$= \frac{1}{N^2}\sum_{p,q=1}^{p,q=N} \langle |\mathbf{a}_p(s)|^2 |\mathbf{a}_q(s + \mathbf{r})|^2\rangle$$
$$= \frac{1}{N^2}\sum_{p,q=1}^{p,q=N} [\langle |\mathbf{a}_p(s)|^2\rangle\langle |\mathbf{a}_q(s + \mathbf{r})|^2\rangle$$
$$+ |\langle \mathbf{a}_p(s)\mathbf{a}_q{}^*(s + \mathbf{r})\rangle|^2], \qquad (4)$$

where we used a fundamental property of zero-mean circular symmetric Gaussian processes in the third equality, and the intensities $I_p(s)$, with $p \in \{1, \ldots, N\}$, and $I_q(s + \mathbf{r})$, with $q \in \{1, \ldots, N\}$, are the one-look intensities used to form the N-look intensities I_s and $I_{s+\mathbf{r}}$, respectively. The corresponding one-look complex amplitudes $\mathbf{a}_p$ and $\mathbf{a}_q$ are such that

$$\langle |\mathbf{a}_p(s)|^2\rangle = \langle I \rangle_l \int |h_p(\mathbf{x})|^2 T_l(s - \mathbf{x})d\mathbf{x}, \qquad (5)$$

where $d\mathbf{x}$ is an elementary displacement in the image plane and h_p is the product of convolution of the system coherent impulse response h with the multilooking filter f_p used to select the one-look complex sample $\mathbf{a}_p$ from the available SAR bandwidth. By using Eq. (5), we see that from Eq. (4)

$$R_{I_l}(s, s + \mathbf{r}) = \frac{\langle I \rangle_l{}^2}{N^2}\sum_{p,q=1}^{p,q=N}\left[\left\langle \iint |h_p(\mathbf{x})|^2 |h_q(\mathbf{y})|^2 \right.\right.$$
$$\times T_l(s - \mathbf{x})T_l(s + \mathbf{r} - \mathbf{y})d\mathbf{x}d\mathbf{y}\Big\rangle$$
$$+ \left\langle \iint h_p(\mathbf{x})h_p{}^*(\mathbf{x} - \mathbf{r})h_q{}^*(\mathbf{y})h_q(\mathbf{y} - \mathbf{r}) \right.$$
$$\left.\left. \times T_l(s + \mathbf{r} - \mathbf{x})T_l(s + \mathbf{r} - \mathbf{y})d\mathbf{x}d\mathbf{y}\right\rangle\right]. \qquad (6)$$

Although in practice the impulse responses h_p, with $p \in \{1, \ldots, N\}$, may differ slightly in magnitude, we assume that they are nearly all equal to an impulse response denoted h_N. When the one-look complex samples used for multilooking are independent, $\mathbf{a}_p$ and $\mathbf{a}_q$ are independent zero-mean random processes, unless p equals q, and Eq. (6)

becomes

$$R_{I_l}(s, s + \mathbf{r}) = \langle I \rangle_l^2 \left\langle \int\int |h_n(\mathbf{x})|^2 |h_N(\mathbf{y})|^2 \right.$$

$$\times T_l(s - \mathbf{x})T_l(s + \mathbf{r} - \mathbf{y})\mathbf{dxdy} \right\rangle$$

$$+ \frac{\langle I \rangle_l^2}{N} \left\langle \int\int h_N(\mathbf{a})h_N{}^*(\mathbf{a} - \mathbf{r})h_N{}^*(\mathbf{b})h_N(\mathbf{b} - \mathbf{r}) \right.$$

$$\times T_l(s + \mathbf{r} - \mathbf{a})T_l(s + \mathbf{r} - \mathbf{b})\mathbf{dadb} \right\rangle. \quad (7)$$

Similar expressions were derived previously.[18,19] We will go further by examining the case in which T_l varies slowly compared with the spatial width of the impulse response h_N. In any case, if the texture features of interest in the scene are spatially smaller than the width of h_N, multilooking will probably smooth them out. By using this assumption and dropping the index s for simplicity (T_l has stationary statistics), we rewrite Eq. (7) as

$$R_{I_l}(\mathbf{r}) = \langle I \rangle_l^2 R_{T_l}(\mathbf{r})|R_{h_N}(0)|^2 + \langle I \rangle_l^2 R_{T_l}(0)\frac{|R_{h_N}(\mathbf{r})|^2}{N}. \quad (8)$$

As $|R_{h_N}(0)|^2$ is one and $R_{T_l}(\mathbf{r})$ may be replaced by $(1 + \rho_{T_l}(\mathbf{r})\sigma_{T_l}^2)$, where ρ_{T_l} is the texture autocorrelation coefficient and $\sigma_{T_l}^2$ is the variance of texture, the autocovariance of the intensity C_{I_l} [that is, $C_{I_l}(\mathbf{r}) = R_{I_l}(\mathbf{r}) - \langle I \rangle_l^2$] is

$$C_{I_l}(\mathbf{r}) = \langle I \rangle_l^2 \left[\rho_{T_l}(\mathbf{r})\sigma_{T_l}^2 + (1 + \sigma_{T_l}^2)\frac{|R_{h_N}(\mathbf{r})|^2}{N} \right]. \quad (9)$$

When there is no texture in the SAR scene, σ_{T_l} is zero in Eq. (9). As $|R_{h_N}(\mathbf{r})|^2$ is nearly zero after a displacement of one to two pixels[2] because of sampling of the SAR data versus the spatial width of h_N, $C_{I_l}(\mathbf{r})$ is nearly zero for a displacement $\mathbf{r}$ greater than or equal to one pixel spacing and N greater than one, and the multilook SAR intensities are nearly uncorrelated. Hence, Eq. (9) shows that the contribution of image speckle to the correlation of multilook SAR intensity data decreases rapidly and significantly with an increasing number of looks and an increasing displacement in pixels.

When texture is present, the first term on the right-hand side of Eq. (9) becomes dominant, provided that

$$N \gg \frac{1 + \sigma_{T_l}^2}{\sigma_{T_l}^2}. \quad (10)$$

This is expected because, for N large, image speckle does not dominate the statistics of the signal, and the SAR intensity image resembles an incoherent image of the radar cross section of the remotely sensed surface. The autocovariance of the intensity $C_{I_l}(\mathbf{r})$ is then equal to the autocovariance of texture modulated by $\langle I \rangle_l^2$.

In the case of the actual SAR data used in this study (see Section 8), N is 3.2 and $\sigma_{T_l}^2$ is much smaller than 0.3 in all regions. The multilook intensities are therefore nearly uncorrelated according to Eq. (9). Direct measurements of the autocovariance of the intensity $C_{I_l}(\mathbf{r})$ (not shown in this paper) confirm this result. One reason for this is that the number of looks is not large enough to reduce image speckle sufficiently and to reveal the natural textural variability of the backscatter cross section of the surface. Another reason is that the measured low values of $\sigma_{T_l}^2$ indicate that the spatial resolution of the SAR data, ~15 m on the ground, is not fine enough to sample correctly the texture features that might be present in the scene.

We conclude that, unless the number of looks is large or the variance of texture is large, the spatial correlation of the multilook SAR intensity data in each homogeneous region of the scene is negligible. This conclusion does not mean that the scene itself is textureless because a spatial variability of the intensity is still present at the transition boundary between different regions (that is, change in the region labeled l).

When the SAR imaging and processing systems are out of focus because of processing errors, the processed SAR image is blurred. However, misfocusing affects only the coherency of the imaged scene, and image speckle remains the same.[17] Misfocusing is hence equivalent to a spatial smoothing of the texture random variable T_l in Eq. (9), that is, texture features are less visible in the SAR scene, $\sigma_{T_l}^2$ decreases, ρ_{T_l} is more nearly uniform, and C_{I_l} is closer to zero.

When the one-look complex samples used for multilooking are uncorrelated, the detected intensity samples are independent and so are the multilook intensity samples. When the single-look complex amplitude data are correlated, in the limit of an infinite number of looks, uncorrelated multilook intensity samples are independent because they are Gaussian distributed. In the case of a finite number of looks, although the assumption is not mathematically correct for gamma distributions, we assume that uncorrelated multilook intensity samples are also mathematically independent. The joint distribution of $\mathbf{I}_s = \{I_i\}_{i \in N_s}$ is hence approximated by the product of the marginal distributions as

$$p(\mathbf{I}_s/L_s) \propto \exp[-MU_1(\mathbf{I}_s/L_s)], \quad (11)$$

where M is the number of pixel elements contained in N_s and, with the use of Eq. (1), the energy function U_1 is

$$U_1(\mathbf{I}_s/L_s) = \frac{1}{M} \sum_{i=1}^{i=M} \left[\frac{NI_i}{\langle I \rangle_{L_s}} - (N - 1)\log(I_i) \right]$$
$$+ N \log(\langle I \rangle_{L_s}). \quad (12)$$

In the actual SAR data used in this study (see Section 8), N is constant and independent of the regions so that each region of the image is uniquely characterized by its mean intensity level $\langle I \rangle_l$.

A valid concern is to verify that using an uncorrelated statistical model of the multilook intensity data negligibly reduces classification accuracy compared with using a correlated image model. We consider the case of one-look intensity data because errors caused by simplifying model assumptions are expected to be greatest in that case since one-look SAR complex amplitudes are strongly correlated. The one-look SAR complex observations of sea ice used in Rignot and Chellappa[2] are detected and classified by assuming uncorrelated intensity samples, as proposed in this paper. The classification results are shown in Fig. 1. The maximum likelihood (ML) classification map, shown in Fig. 1(a), is comparable with the minimum distance (MD) classification map (Fig. 5b of Ref. 2). This result is expected because the one-look intensity samples are strongly correlated. However, when the MAP classifier is
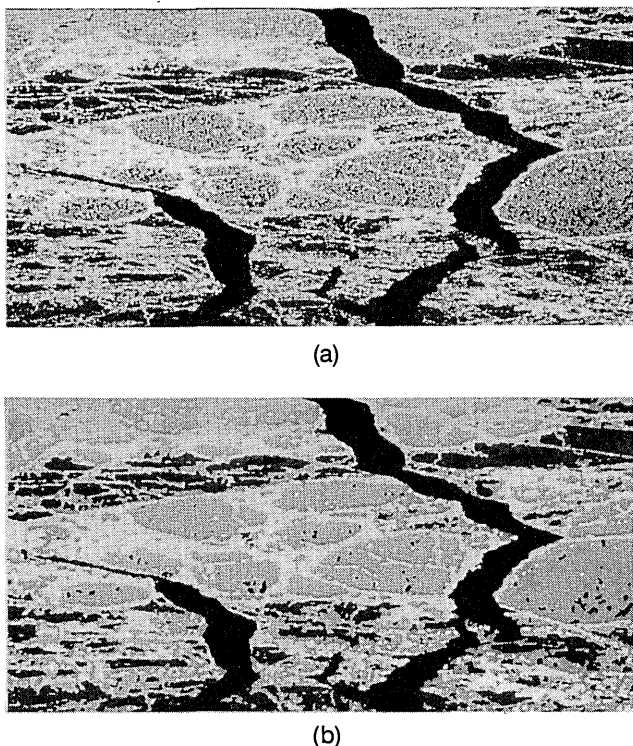
(a)

(b)

Fig. 1. Classification map of one-look SAR observations of sea ice at L-band HH polarization assuming uncorrelated samples and using (a) a ML classifier, (b) a MAP classifier. In decreasing order of brightness are ice ridges, multiyear ice, first-year ice, and thin ice.

used, the resulting classification map [Fig. 1(b)] resembles quite well the classification map obtained when a fully correlated model is used (Fig. 5f of Ref. 2). Only 5% of the pixels are labeled differently in the two results. As the difference in classification quality is expected to decrease with an increasing number of looks because neighboring samples will be less correlated, this example illustrates that the uncorrelated assumption does not significantly reduce the performance of the MAP classifier on multilook intensity data. In fact, this assumption may be a reasonable approach even with one-look intensity data.

Further arguments justify the use of a simple analytical model for the joint distribution of multilook SAR intensity data. In most current and future multilooking SAR processors for spaceborne SAR instruments, multilook SAR intensity data will be resampled automatically and mapped onto an Earth-fixed grid. These resampling and geo-referencing processes, known as geocoding,[20] facilitate the incorporation and registration of SAR data with data acquired by other sensors that are complementary to SAR and necessary to science applications.[8] As SAR geocoding is a nonlinear and range-variant process, it introduces severe nonlinearities in the first- and second-order statistics of the multilook intensity data. Thus the accurate analytical modeling of the autocorrelation function of the multilook intensities becomes too complicated for practical image classification.[18]

B. Prior Distribution of the Region Labels
An MRF model is used for representing the spatial interactions between neighboring region labels as in Ref. 2. The conditional prior distribution of region label L_s of

pixel site s given the region labels L_r of the neighbors of s contained in N_s is modeled as

$$p(L_s/L_r, r \in N_s) = \frac{1}{Z_2} \exp[-M U_2(L_s/L_r, r \in N_s)], \quad (13)$$

where the Gibbs energy function U_2 is

$$U_2(L_s/L_r, r \in N_s) = -\frac{\beta}{M} \sum_r \delta_k(L_s - L_r), \quad (14)$$

β is a clustering parameter equal to 1.4, Z_2 is a normalizing constant independent of L_s, and $\delta_k(L_s - L_r)$ is the Kronecker delta. Equation (13) models region labeling as an isotropic process, with local dependences only, and with a degree of clustering of the region labels, parametrized by β, independent of the regions. The conditional prior distribution of L_s is an exponential function of the number of like pairs of region labels within N_s. In Rignot,[21] the results obtained with this kind of distribution are nearly identical to those obtained when using a conditional prior distribution of L_s directly proportional to the number of like pairs of region labels in N_s. This observation indicates that the most physically relevant feature of Eq. (13) is not so much the particular shape of the prior distribution of L_s but the level of spatial dependence assumed for the region labels, that is, the parameters β and M. The advantage of an exponential distribution is that it subsequently yields a simpler expression of the MAP criterion.

3. MAXIMUM *A POSTERIORI* CLASSIFIER

From Bayes's theorem, the posterior distribution of the region label array $\mathbf{L} = (L_s)_{s \in \Omega}$ given the SAR intensity array $\mathbf{I} = (I_s)_{s \in \Omega}$ is

$$p(\mathbf{L}/\mathbf{I}) = \frac{p(\mathbf{L})p(\mathbf{I}/\mathbf{L})}{p(\mathbf{I})}. \quad (15)$$

As $\mathbf{I}$ is known, the denominator is just a positive constant. If the intensity array Ω is viewed as composed of a set of overlapping windows N_s centered at each pixel location s such that each window is homogeneous (that is, all pixels have the same region label), given that the multilook SAR intensities are independent, the prior distribution of the intensity array is

$$p(\mathbf{I}/\mathbf{L}) = \prod_s p(\mathbf{I}_s/L_s). \quad (16)$$

With proportionality (11) and Eqs. (13) and (16), Eq. (15) becomes

$$p(\mathbf{L}/\mathbf{I}) \propto \exp -\left\{ M \sum_s [U_1(\mathbf{I}_s/L_s) + U_2(L_s/L_r)] \right\}. \quad (17)$$

The estimate of $\mathbf{L}$ that maximizes $p(\mathbf{L}/\mathbf{I})$, is Bayes's optimum or most likely estimate of the region labels given the SAR data or its MAP estimate. In our model, the MAP estimate minimizes the energy function

$$E_{\mathrm{MAP}} = \sum_s [U_1(\mathbf{I}_s/L_s) + U_2(L_s/L_r)]. \quad (18)$$

The minimization of Eq. (18) is performed on a parallel

Table 1. Percentage Error of the MAP Classifier for N-look Intensity SAR Data versus the Texture Parameter α

N look	ML ($\alpha = \infty$)	MAP ($\alpha = \infty$)	ML ($\alpha = 1$)	MAP ($\alpha = 1$)
1	30.8	4.0	33.0	12.2
2	24.3	0.8	29.5	3.6
4	18.7	0.7	24.9	1.6
8	11.2	0.6	16.7	1.0

optimization network identical to the one described by Rignot and Chellappa[2] when either the iterated conditional modes algorithm for fast convergence to an approximate solution or the simulated annealing technique for slower convergence to a more accurate solution is used.

4. PERFORMANCE USING COMPUTER-SIMULATED SAR IMAGERY

Multilook SAR intensity data are simulated on the computer by using the technique described by Rignot and Chellappa[2] for generating one-look SAR complex amplitude data. To form an N-look intensity sample, we incoherently average N independent one-look DAR complex amplitudes. The mean intensity level $\langle I \rangle_l$ is a gamma-distributed random variable of parameter α_l to simulate the texture variability of the radar cross section of the surface. The simulated N-look images are 128×128 pixels in size and comprise two regions, 64×128 pixels in size, corresponding to two different intensity levels I_0 and I_1.

Table 1 gives the classification error (that is, the percentage of misclassified pixels in the image) of the simulated SAR intensity data as a function of the number of independent looks N for several intensity classifiers when the contrast between the regions is 2 dB. These intensity classifiers are an MD classifier, an ML classifier [equivalent to $\beta = 0$ in Eq. (14)] and a MAP classifier. The classification error is shown to decrease significantly with an increasing number of looks in all cases. This decrease is expected because when the number of looks increases, the variance of the SAR signal decreases, and so does the probability of error of the classifier.[22] Hence, multilook intensity data yield better classification accuracies than one-look complex amplitude data when the regions are homogeneous. Increasing the number of looks, however, decreases spatial resolution and the relevance of the synthetic aperture technique. The results in Table 1 also show that the MAP technique performs 10–25% better than does the ML technique when the contrast between regions is 2 dB. This significant difference justifies the use of the MAP technique, as in many real applications

the contrast between surfaces of importance is only of the order of a few decibels. Finally, the results obtained with the one-look complex amplitude data, also shown in Table 1, indicate that using the correlation of the complex amplitudes (ML complex) decreases the classification error by 5% compared with the case when the one-look SAR intensity data are assumed uncorrelated (ML intensity) but that little or no difference exists between the two methods when the MAP classifier is used.

Table 2 shows the classification error of the ML and MAP classifiers for two values of the texture parameter α_l. α_l infinite corresponds to $\langle I \rangle_l$ being a constant, and α_l equal to one corresponds to $\langle I \rangle_l$ being exponentially distributed. The results show that the presence of texture does not significantly decrease the performance of the MAP classifier, even in the presence of a strong spatial variability of the signal ($\alpha = 1$).

The effect on classification error of an underestimation of N is equivalent to that of the selection of a larger value of β, that is, to more smoothing of the region labels [see Eq. (18)]. When N is overestimated, less smoothing is operated on the region labels. As β may vary by as much as 30% without significant effects on classification accuracy,[2] N does not need to be known with an accuracy better than 30% in real applications.

5. GENERALIZATION TO THE MULTIFREQUENCY CASE

The complex amplitudes of radar returns from the same resolution cell acquired at two different operating frequencies of the radar system are uncorrelated. One reason for this is that the radar signal is sensitive to scatterers of a different nature. The penetration depth of the radar signal changes with frequency. Longer wavelengths penetrate deeper into the surface cover (soil or vegetation). The penetration of the signal is accompanied by a change in the dielectric constant of the reflecting material because the surface composition changes with depth, by a change in the roughness scale of the reflecting surface because of a change in the radar wavelength, and by a change in incidence angle because of refraction.[23] As a result, the observed backscatter cross sections are uncorrelated. Furthermore, image speckle (which modulates the backscatter cross sections in the received signal) is uncorrelated between the two frequencies because the spectra corresponding to the two data takes do not overlap, resulting in a product of the spectra equal to zero, that is, uncorrelated data. It is for the same reason that multilooking based on spectral division[4] works for reducing image speckle. In effect, the one-look spectra selected for

Table 2. Percentage Error of Several Classifiers versus the Number of Looks N When Using Computer-Simulated SAR Data: Minimum Distance Using Intensities (MD Intensity), Maximum Likelihood Using Intensities (ML Intensity), Maximum a *Posteriori* Using Intensities (MAP Intensity), Maximum Likelihood Using Complex Amplitudes (ML Complex), and Maximum a *Posteriori* Using Complex Amplitudes (MAP Complex)

N	MD Intensity	ML Intensity	MAP Intensity	ML Complex	MAP Complex
1	30.7	30.8	4.0	25.1	4.0
2	29.5	24.3	0.8	–	–
4	24.9	18.7	0.7	–	–
8	16.7	11.2	0.6	–	–

multilooking do not overlap, resulting in independent sample images or looks of the scene. Therefore, the frequency separation criterion for obtaining uncorrelated SAR measurements is that the difference in frequency between f_1 and f_2 must be larger than the SAR bandwidth of each data take. In practice, multifrequency remote-sensing radars operate at frequencies that are separated by several gigahertz, whereas typical SAR bandwidth are less than 1 GHz. So the frequency separation criterion is always verified.

Because uncorrelated circular Gaussian complex amplitudes are also independent, the joint distribution of M multifrequency measurements is the product of the M marginal distributions for each frequency. In the case of multilook SAR intensity data acquired at two frequencies, f_1 and f_2, we assume that the uncorrelated multifrequency intensity samples are also independent and that

$$p(\mathbf{I}_s^{f_1}, \mathbf{I}_s^{f_2}/L_s) \propto \exp -\{M[U_1(\mathbf{I}_s^{f_1}/L_s) + U_1(\mathbf{I}_s^{f_2}/L_s)]\}. \quad (19)$$

The resulting energy function is the sum of the energy functions for each frequency. As the model for the region labels remains the same, the MAP estimate of the region labels minimizes

$$E_{\mathrm{MAP}} = \sum_s [U_1(\mathbf{I}_s^{f_1}/L_s) + U_1(\mathbf{I}_s^{f_2}/L_s)] + U_2(L_s/L_r)]. \quad (20)$$

In Eq. (20), each additional frequency considered during classification of the SAR scene adds a bias input current to each node of the optimization network,[2] minimizing E_{MAP}. If the additional channels are indeed informative, the energy function U_1 will increase compared with U_2 in Eq. (20), that is, less smoothing of the region labels will be effected. This is expected, as the MAP labeling technique uses the information content of the data and does not perform a simple blind smoothing of the region labels.
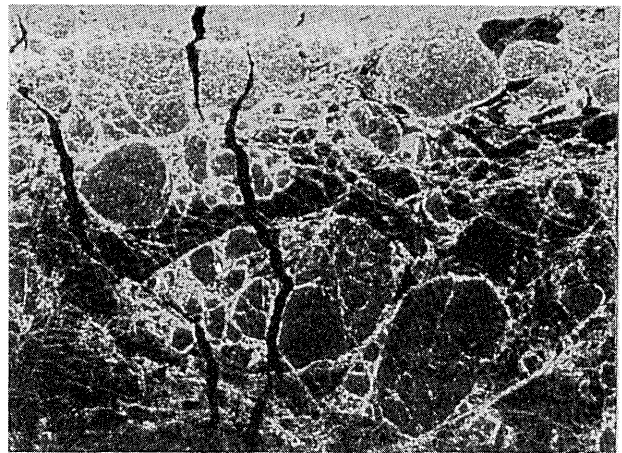
6. ADAPTATION TO INCIDENCE ANGLE EFFECTS

The radar cross section of natural surfaces depends on the incidence angle θ_i of the radar electromagnetic wave onto the surface. The incidence angle varies over the surface to be imaged because of the SAR imaging geometry (areas nearer the radar will be imaged at a steeper incidence angle) and because of spatial variations in surface slopes owing to the presence of topography (surface slopes facing the radar will correspond to steeper incidence angles than surface slopes away from the radar). In the case of the SAR data acquired by the NASA/JPL airborne SAR (AIRSAR), θ_i typically varies between 22° and 52° across range when a surface with negligible variations in surface slopes is imaged, and typical variations in radar backscatter may easily exceed 6 dB across range. For any classifier to work correctly on SAR imagery, it is therefore essential to incorporate incidence angle effects.

In Eq. (12), $\langle I \rangle_l$ depends on θ_i. Hence, to compute the energy function U_1, we must generate a lookup table of the values of $\langle I \rangle_l$ as a function of θ_i, and θ_i must be computed for each image pixel to use the correct value of $\langle I \rangle_l$. All pixels in the neighborhood N_s of pixel s are assumed to have the same value of $\langle I \rangle_l$ as θ_i varies only by fractions of a degree within N_s. When the changes in incidence angle
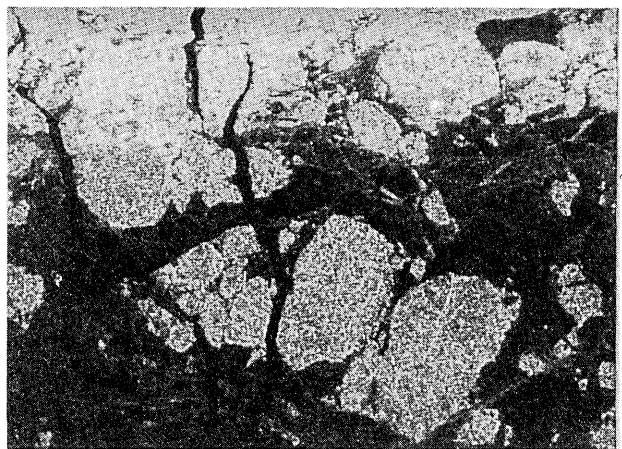
owing to local surface slopes produce negligible changes in radar cross section (flat surface), θ_i is constant for each range line, and the process of accounting for changes in incidence angle does not significantly increase the computation time. The energy function U_2 of the region labels does not depend on θ_i. As U_1 is computed once during the classification process and U_2 is the only function that is iteratively adjusted during optimization of the region labels, the computation time of the MAP classifier is nearly unchanged when the image characteristics are varying within the image owing to incidence angle effects.

7. EXAMPLES USING AIRSAR DATA

Multilook SAR intensity images of sea ice acquired by AIRSAR in March 1988 in the Beaufort Sea, north of Alaska, are shown in Fig. 2. Near range is on top, the aircraft flying from right to left in the figure. The images are 1024×750 pixels in size; pixel spacing is 6.7 m in slant range and 12.1 m in azimuth. The SAR data are processed four looks, but the effective reduction in variance of image speckle is approximately $N = 3.2$ because the one-look data used for multilooking are slightly correlated. The value of N is computed accurately from the

(a)

(b)

Fig. 2. Total power image of four-look SAR intensity observations of sea ice acquired by AIRSAR over the Beaufort Sea, north of Alaska, at (a) L-band frequency, HH polarization, (b) C-band frequency, VV polarization.
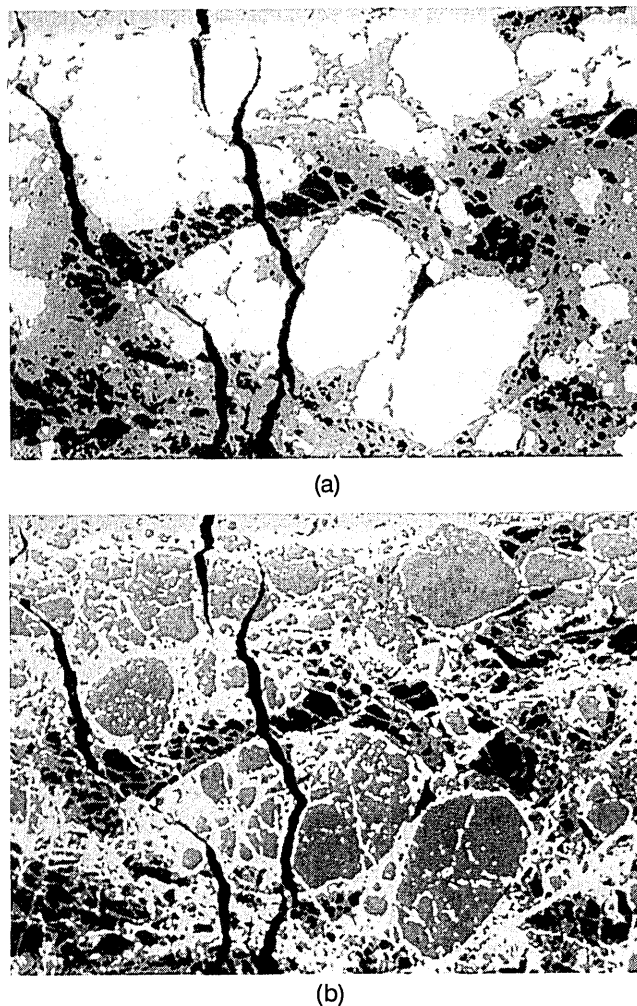
(a)

(b)

Fig. 3. Classification map of the SAR intensity data of Fig. 2 by using a MAP classifier. (a) C-band VV polarization: MY and CFY are white, FYR is light gray, FYS is dark gray, ThI is black. (b) L-band HH polarization: CFY is white, MY and FYR are light gray, FYS is dark gray, and ThI is black. Abbreviations are defined in text.

correlation of the one-look complex samples used to form the multilook image by using an expression given by Zelenka.[4] The incidence angle θ_i varies between 22° (near range, top in Fig. 2) and 52° (far range, bottom in Fig. 2). Figure 2(a) shows the SAR image at L-band frequency (24-cm wavelength) and HH polarization (that is, horizontal transmit and horizontal receive polarizations). Figure 3 shows the same scene at C-band frequency (5.6-cm wavelength) and VV polarization (that is, vertical transmit and vertical receive polarizations). The data were processed such that the multifrequency SAR measurements are spatially registered. These two modes of radar operation correspond, respectively, to that of the Japanese First Earth Resources Satellite J ERS-1 (L-band HH) launched in February 1992 and of the European First Remote Sensing Satellite ERS-1 (C-band VV) launched in July 1991. C-band VV separates well the multiyear-old sea ice [bright floes in Fig. 2(b)] and first-year sea ice [darker ice in Fig. 2(b)] but does not quite show the pressure ridges in the ice. L-band HH reveals pressure ridges and ridge lines in the ice [bright linear features in Fig. 2(a)] but confuses ridges and multiyear sea ice. Thin ice appears dark at both frequencies in a frozen lead run-

ning across the image from top to bottom. Separation of these different sea-ice types is important, as each ice type is related to a typical range of ice thickness and ice thickness is a major control parameter in the modeling of the heat flux between the oceans and the atmosphere.[8] The distribution of sea-ice pressure ridges is useful when one is estimating the surface atmospheric drag coefficient in climate modeling over the polar regions, studying acoustic sources in the ice sheet, or guiding ships through safer routes since ice breakers often cannot go through pressure ridges without damaging the ship.[24]

A detail mapping of the different sea-ice types present in the scene is given by Rignot and Drinkwater[25] on the basis of a combination of multifrequency and multipolarization SAR data, passive microwave data, limited surface observations of the ice, and meteorological observations collected at a nearby ice camp. The backscatter characteristics of five sea-ice types were extracted across range. These ice types are compressed first-year sea ice (CFY); multiyear sea ice (MY); first-year ridge and rubble ice (FYR); first-year smooth sea ice (FYS); and thin ice (ThI). A summary of the radar backscatter characteristics of these ice types is given in Table 3 at L-band HH and C-band VV and θ_i equal to 45°. Measurements of the spatial variability of the signal (not shown in the paper but available in Ref. 21) indicate only a small texture variability of the signal ($\sigma_T^2 \ll 1$) and an autocovariance of the intensity C_I close to zero. Hence, despite the highly textured appearance of the SAR images, most of the signal variability is due only to image speckle or to transitions to a different sea-ice type, and the intensity samples are nearly uncorrelated.

The computation of the energy function $U_1(\mathbf{I}_s/L_s)$ for the different classes at each pixel location is performed by using Eq. (12) with $\langle I \rangle_l$ being dependent on the incidence angle. During optimization of the region labels, $U_2(L_s/L_r)$ is computed for each pixel and iteratively adjusted by using an optimization network.[2] The MAP classification maps corresponding, respectively, to L-band HH and C-band VV are shown in Fig. 3. The classification accuracy of the dif-

Table 3. Backscatter Characteristics Expressed in Decibels of Five Different Sea-Ice Types at L-Band HH Polarization and C-Band VV Polarization and for $\theta_i = 45°$

Ice Type	$\sigma°$ at L-band HH (dB)	$\sigma°$ at C-band VV (dB)
ThI	−35.9	−26.0
FYS	−26.2	−20.6
FYR	−23.2	−19.1
MY	−23.0	−11.8
CFY	−17.7	−12.1

Table 4. Confusion Matrix in Percentage Points of Different Sea-Ice Types at C-Band VV Polarization When the MAP Classifier Is Used

Ice Type	ThI	FYS	FYR	MY	CFY
ThI	97	17	1	0	0
FYS	3	54	15	0	0
FYR	0	29	83	1	16
MY	0	0	1	51	35
CFY	0	0	0	48	49

Table 5. Confusion Matrix in Percentage Points of Different Ice Types at L-Band HH Polarization When the MAP Classifier Is Used

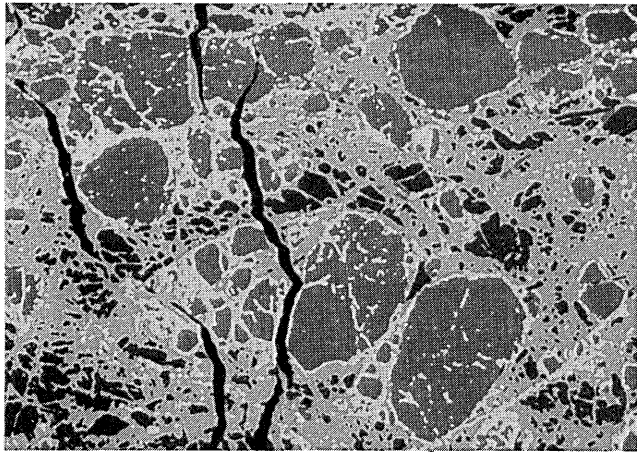| Ice Type	ThI	FYS	FYR	MY	CFY
ThI	98	13	0	0	0
FYS	2	83	8	1	0
FYR	0	3	65	32	31
MY	0	1	21	68	4
CFY	0	0	6	0	64

Fig. 4. Classification map of the SAR intensity data of Fig. 2 by using a MAP classifier at L-band HH polarization and C-band VV polarization combined: CFY is white, FYR is light gray, MY is gray, FYS is dark gray, and ThI is black.

Table 6. Confusion Matrix in Percentage Points of Different Ice Types at L-Band HH Polarization and C-Band VV Polarization Combined When the MAP Classifier Is Used

Ice Type	ThI	FYS	FYR	MY	CFY
ThI	99	11	0	0	0
FYS	1	84	7	0	0
FYR	0	5	91	0	12
MY	0	0	1	98	10
CFY	0	0	1	1	78

ferent ice types is recorded in confusion matrices, which are shown in Table 4. Each confusion matrix indicates how classification inaccuracy results in labeling of pixels in the wrong ice classes, along with the percentage of misclassified pixels. Vertical columns indicate how, for a particular ice class, various pixels are misclassified. Each vertical column totals 100%, and components of each vertical column denote the percentage of misclassification as other classes relative to the correct classification.[25] The MAP classifier is 15–20% better than the ML classifier (not shown in Fig. 3), which ignores spatial context and assumes equal *a priori* probabilities for the regions and therefore a significant improvement in classification accuracy.

The results in Table 4 show that C-band VV separates ThI, FYS, and FYR but confuses CFY and MY. CFY and MY have been represented with the same gray level in Fig. 3(a). As MY and CFY both correspond to thicker ice types, the error introduced at C-band VV is not significant for the thermodynamic balance of the area, but the MY/FY ice fraction is overestimated by 15%. In Table 5,

L-band HH is shown to separate MY and CFY better but confuses MY and FYR, which are represented with the same gray level as in Fig. 3(b). The overall classification accuracy (average of the diagonal terms of the confusion matrix) for the entire scene is 68% at C-band VV and 75% at L-band HH.

The MAP classification at L-band HH and C-band VV combined is shown in Fig. 4. Pressure ridges are better detected than in the single-frequency case, and MY and FY are better separated. The confusion matrix, shown in Table 6, gives an overall classification accuracy of the five sea-ice types of 89%, that is, 15–22% higher than in the single-frequency case. The distribution and geometric characteristics of the MY ice floes appear clearly in the classification map, and we can retrieve the spatial distribution of pressure ridges.

8. CONCLUSIONS

This paper presents a Bayesian MAP classifier for multifrequency, multilook SAR intensity data based on a model of the posterior distribution of the region labels of the image, given multifrequency, multilook SAR observations. We showed that the assumption of spatially uncorrelated SAR intensity samples is a reasonable assumption that does not significantly affect classification accuracy. Classification accuracy increases with an increasing number of looks and is robust to the presence of a texture variability of the radar cross section of natural surfaces. The technique is applicable to incidence angle dependent image characteristics. An example of application using actual SAR data showed significant gain in classification accuracy resulting from the combination of several frequencies. The technique could be used to classify spaceborne SAR data collected by ERS-1 and J ERS-1. As a further extension of this work, Rignot and Chellappa[26] presented a Bayesian MAP classifier for polarimetric SAR data acquired at one frequency. In that case, the correlation between the different polarimetric channels of the radar system is essential to separate different types of natural surfaces, and modeling of the statistical distribution of the SAR measurements is significantly different.

REFERENCES

1. D. L. Evans and O. S. Milton, "Separation of vegetation and rock signatures in thematic mapper and polarimetric SAR images," Remote Sens. Environ. **37**, 63–75 (1991).
2. E. Rignot and R. Chellappa, "Segmentation of synthetic-aperture-radar complex data," J. Opt. Soc. Am. A **8**, 1499–1511 (1991).
3. J. C. Curlander and R. N. McDonough, *Synthetic Aperture Radar: Systems and Signal Processing,* J. Kong, ed., Wiley Series in Remote Sensing (Wiley, New York, 1991).
4. J. Zelenka, "Comparison of continuous and discrete mixed-integrator processors," J. Opt. Soc. Am. **66**, 1295–1304 (1976).

5. L. J. Porcello, N. G. Massey, R. B. Innes, and J. M. Marks, "Speckle reduction in synthetic aperture radars," J. Opt. Soc. Am. **66,** 1305–1311 (1976).

6. J. S. Lee, "Segmentation of SAR imagery, "IEEE Trans. Geosci. Remote Sens. **27,** 674–680 (1989).

7. R. M. Haralick, S. K. Shanmugan, and I. Dinstein, "Textural features for image classification," IEEE Trans. Syst. Man Cybern. **SMC-3,** 610–621 (1973).

8. *Earth Observing System,* Synthetic Aperture Radar Instrument Panel Rep. (National Aeronautics and Space Administration, Washington, D.C., 1988), Vol. IIf.

9. D. L. Evans, J. J. van Zyl, and C. F. Burnette, "Incorporation of polarimetric radar images into multisensor data sets," IEEE Trans. Geosci. Remote Sens. **28,** 932–939 (1990).

10. F. T. Ulaby and M. C. Dobson, *Handbook of Radar Scattering Statistics for Terrain* (Artech, Norwood, Mass., 1989).

11. J. W. Goodman, "Statistical properties of laser speckle patterns," in *Laser Speckle and Related Phenomena,* J. C. Dainty, ed., Vol. 9 of Topics in Applied Physics (Springer-Verlag, New York, 1975), pp. 9–75.

12. E. Jakeman and R. J. A. Tough, "Generalized K-distribution: a statistical model for weak scattering," J. Opt. Soc. Am. A **4,** 1764–1772 (1987).

13. J. K. Jao, "Amplitude distribution of composite terrain radar clutter and the K-distribution," IEEE Trans. Antennas Propag. **AP-32,** 1049–1062 (1984).

14. E. Jakeman and P. Pusey, "A model for non-Rayleigh sea echo," IEEE Trans. Antennas Propag. **AP-24,** 806–814 (1976).

15. S. H. Yueh, J. A. Kong, J. K. Jao, R. T. Shin, and L. M. Novak, "K-distribution and polarimetric terrain radar clutter," J. Electromag. Waves Appl. **3,** 747–768 (1989).

16. H. Laur, "Analyse d'images radar en teledetection: discriminateurs radiometriques et texturaux," Ph.D. dissertation 403 (Université Paul Sabatier de Toulouse, Toulouse, France, 1989).

17. R. K. Raney, "Transfer functions for partially coherent SAR systems," IEEE Trans. Aerosp. Electron. Syst. **AES-19,** 740–750 (1983).

18. S. Madsen, "Spectral properties of homogeneous and non-homogeneous radar images," IEEE Trans. Aerosp. Electron. Syst. **AES-23,** 583–588 (1987).

19. C. Oliver, "The interpretation and simulation of clutter textures in coherent images," Inverse Problems **2,** 481–518 (1986).

20. J. C. Curlander, R. Kwok, and S. Pang, "A post-processing for automated rectification and registration of spaceborne SAR imagery," Int. J. Remote Sens. **8,** 621–638 (1987).

21. E. Rignot, "Segmentation of multifrequency and polarimetric synthetic aperture radar data," Ph.D. dissertation (University of Southern California, Los Angeles, Calif., 1991).

22. S. Madsen, "Speckle theory: modelling, analysis, and applications related to synthetic aperture radar data," Ph.D. dissertation LD62 (Technical University of Denmark, Lynbgy, Denmark, 1986).

23. C. Elachi, *Spaceborne Radar Remote Sensing: Applications and Techniques* (Institute of Electrical and Electronics Engineers, New York, 1988).

24. F. Carsey, "Review and status of remote sensing of sea-ice," IEEE J. Oceanic Eng. **14,** 127–138 (1989).

25. E. Rignot and M. R. Drinkwater, "On the application of multifrequency polarimetric SAR observations to sea-ice classification," in *Proceedings of the International Conference on Geoscience and Remote Sensing* (Institute of Electrical and Electronics Engineers, New York, 1992).

26. E. Rignot and R. Chellappa, "Segmentation of polarimetric synthetic aperture radar data," IEEE Trans. Image Proc. **1,** 281–300 (1992).